npj computational materials

www.nature.com/npjcompumats

ARTICLE OPEN

Check for updates

Realizing unipolar and bipolar intrinsic skyrmions in MXenes from high-fidelity first-principles calculations

Arnab Kabiraj[1] and Santanu Mahapatra[1]✉

Magnetic skyrmions, which are topologically protected tiny spin textures, have emerged as information carriers in energy-efficient logic and memory devices. Skyrmions are commonly realized by inducing large Dzyaloshinskii–Moriya interaction (DMI) in the interface of heavy metal heterolayers. With the advent of two-dimensional magnetism, it is being envisioned to host intrinsic skyrmions in a monolayer, which will be free from any interfacial defect and stacking order. Here using high-fidelity exchange-correlation functional-based first-principles calculations, we investigate such a possibility in methodically designed non-centrosymmetric MXene structures. From a search space of about 3000 materials, our customized high-throughput computational pipeline systematically harnesses out-of-the-plane and in-plane magnetism along with strong DMI to realize typical 'unipolar' skyrmions in 78 materials and exotic 'bipolar' skyrmions in 13 materials. Micromagnetic and atomistic Monte Carlo simulations further reveal that skyrmions in some of these materials may be stable at room temperature without any external magnetic field. Our study may pave the way for the practical realization of skyrmions-based information technology.

npj Computational Materials (2023)9:173 ; https://doi.org/10.1038/s41524-023-01129-x

INTRODUCTION

Skyrmions, topologically protected noncollinear magnetic patterns with spins arranged in a whirl, behave as nanometer-sized quasiparticles and can be manipulated using spin-polarized currents and magnetic fields. Materials with stable skyrmions can be used to fabricate devices that can store and process information at microscopic length scales with ultra-low power consumption[1]. For example, logic 1 and 0 can be represented by the presence/absence of the skyrmion[2]. They have also shown promise in applications of alternative computing paradigms such as reservoir computing[3–7] and neuromorphic computing[8,9]. Other applications are proposed in highly relevant technological areas such as spintronic logic and memory devices[10,11], skyrmion qubits[12], and racetrack memory[13].

Skyrmions were initially identified in liquid crystal[14], and bulk cubic B20 phase crystals without centrosymmetry such as MnSi[15], and (Fe,Co)Si[16]. Later, they were observed in thin films grown on heavy metal surfaces such as Fe/Ir (111)[17]. The loss of inversion symmetry at the surface and large spin-orbit coupling due to the presence of heavy metals and the Rashba effect led to large Dzyaloshinskii–Moriya interactions (DMI), a critical factor for stabilizing skyrmions. Subsequently, ferromagnet/heavy metal heterostructures such as Ir/Fe/Co/Pt[18], Pt/Co/MgO[19] were synthesized to generate large DMIs. Deposition of two-dimensional (2D) materials such as graphene and hBN on Co surfaces has been predicted to result in skyrmion states[20]. However, the DMI is adversely affected by defects at the interface as well as the stacking order of the layers. Designing a single layer of material with inversion asymmetry that creates conditions favorable for stabilizing skyrmions is, therefore, highly desirable. Such 2D materials can be synthesized in a defect-free manner and circumvent the typical issues with bulk materials.

For practical applications in spintronic devices compatible with the current semiconductor technology, the skyrmion phases are desired to be purely controlled by electrical field at room temperature and beyond. However, the room temperature stability of skyrmions has only been observed at finite magnetic fields[21] in the bulk B20 materials or in carefully engineered exchange-biased multilayer stacks[22]. Stabilizing skyrmion phases at higher temperatures (T) without the use of magnetic field (B), poses a great challenge. The finite size effect in 2D layered ferromagnets such as Co-doped Fe_5GeTe_2 can facilitate wide ranges of temperature and magnetic fields for skyrmion stability[23]. High ordering temperatures of about 300 K have also been observed in FeGe thin films at zero magnetic field[24]. Thus, 2D magnetic materials provide immense design possibilities for stabilizing skyrmion phases. It is worth noting that the existence of magnetism in 2D materials was demonstrated experimentally only in 2017[25,26], and since then, 2D magnetism has attracted tremendous attention for its potential use in spintronics[27–29].

Skyrmions, which we have discussed so far, are typically 'unipolar' with an out-of-plane magnetization. Recently, with the help of micromagnetic simulations, it has been hypothesized that even in-plane counterparts of skyrmions may exist in in-plane magnets under certain conditions[30]. This prospect is even more technologically lucrative since these materials can host 'bipolar' skyrmions with both $+1$ and -1 topological charge, a quantity that describes the nature of winding of skyrmions. The conventional out-of-plane skyrmions can exhibit either $+1$ or -1 topological charge, and, therefore, materials hosting the in-plane skyrmions can easily pack 1.5–2 times more information than their conventional out-of-plane counterparts. However, this study does not propose any specific material which may host such bipolar skyrmions. The quest for in-plane skyrmions is, therefore, becoming a highly technologically significant challenge.

With the advancement of computational science and supercomputing technology, in-silico search for application-specific materials has become extremely popular. Since the material space is infinite, experimentally, it is impossible to explore all such possibilities. Therefore, multi-scale computational techniques

[1]Nano-Scale Device Research Laboratory, Department of Electronic Systems Engineering, Indian Institute of Science (IISc) Bangalore, Bengaluru 560012, India.
✉email: santanu@iisc.ac.in

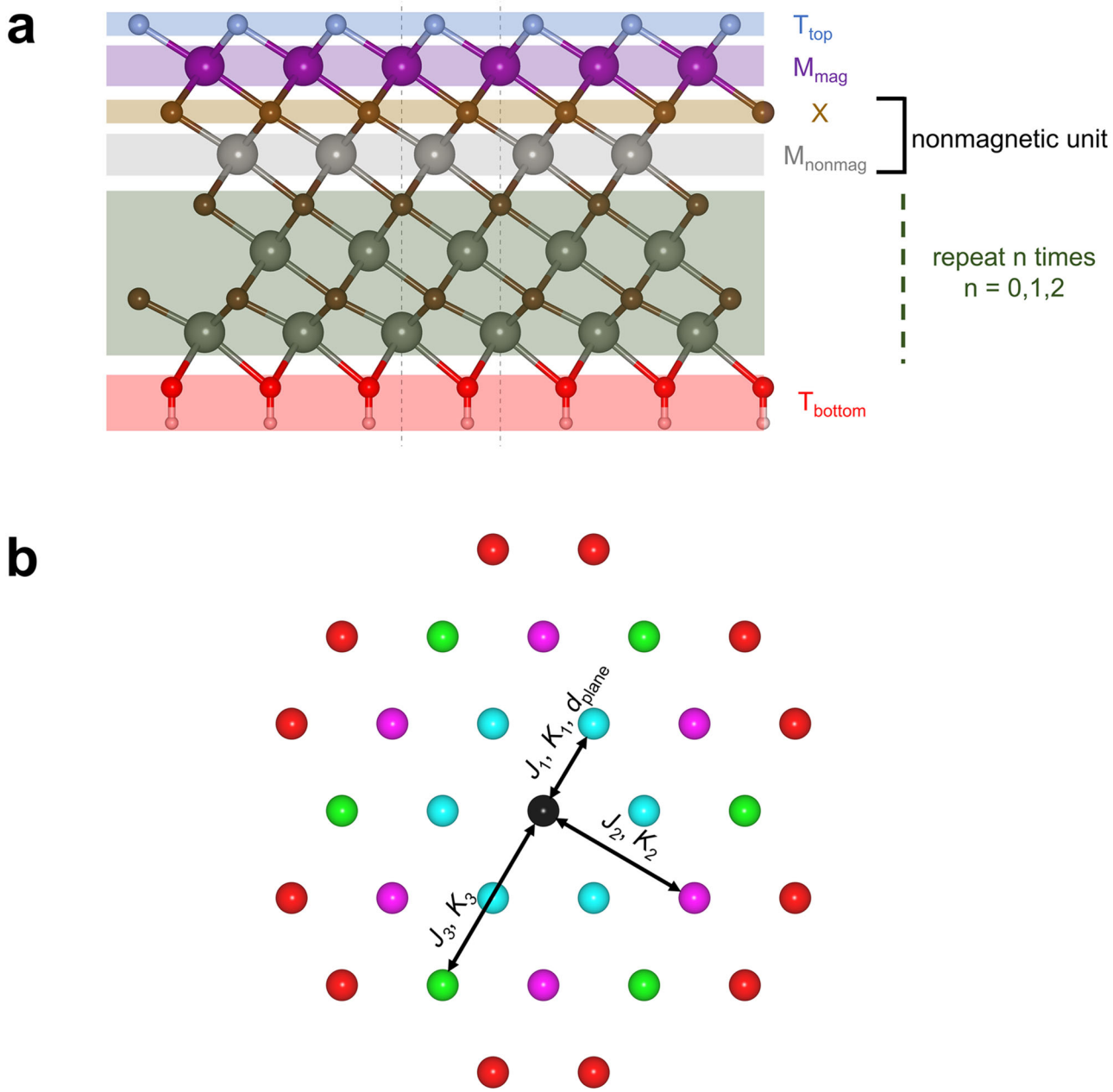

Fig. 1 Anatomy of the MXenes. a The general form of the explored MXenes from a side view is illustrated. **b** The different neighboring shells for the magnetic layer of MXene are shown with a top view of the layer. The 1st, 2nd, 3rd, and 4th nearest neighboring atoms to the central black atom are marked with sky blue, purple, green, and red balls.

involving a combination of first-principles studies, Monte Carlo (MC) simulations, and micromagnetic simulations are essential to discover and design new 2D or layered materials for skyrmion-based applications[31–34]. Among the 2D materials, MXenes, a new group of non-Van der Waals materials, have attracted tremendous attention since their first report of synthesis and characterization in 2011[35], because of their fascinating mechanical and electronic properties[36–38]. MXenes are transition-metal carbides, nitrides, and carbonitrides with the general formula $M_{n+1}X_nT$, in which an early transition metal (M: Ti, Nb, V, Cr, Mo, Ta, etc.) is interleaved with layers of C or N (X), and T indicates surface termination functional groups like OH, = O, and F. Ti_2N, Ti_3C_2, V_4C_3, and Mo_4VC_4 are few examples of MXenes which have been synthesized and characterized[39,40]. With recent advances in the synthesis of ordered or disordered double transition-metal MXenes[41], including the recently introduced method of chemical scissor-mediated structural editing[42], this class of materials is offering unprecedented property tunability with different combinations of metals, Xs, and functional groups. High throughput generic and application-specific computational studies have explored a fraction of this theoretically infinite MXene space[43–49], but properties of most of the possible MXenes remain unknown.

In this work, combining high-fidelity exchange-correlation functional-based first-principles calculations with micromagnetic and Monte Carlo (MC) simulations, we explore a specific subclass of MXenes containing a single magnetic metal layer for the presence of skyrmions. A fully automated high-throughput computational workflow was developed to rigorously scan a large space of around 3000 materials. We end up with 91 promising materials capable of hosting stable skyrmions. We also find a few

materials capable of hosting out-of-plane skyrmions at room temperature without any external magnetic field, which can be useful for designing skyrmion-based devices compatible with the current technology. We also find a few materials capable of hosting the much-coveted bipolar in-plane skyrmions, albeit they exist at a temperature lower than room temperature. Our work might accelerate and aid in the engineering of skyrmion-based spintronics.

RESULTS

Material search space

The DMI effect is strongest in non-centrosymmetric materials. The successful synthesis of ordered and disordered double MXenes has opened a new avenue for non-centrosymmetric 2D materials[41]. Until now, most synthesized MXenes possess 2, 3, and 4 metal layers, barring a single material, Mo_4VC_4, with five metal layers[40]. In addition to the metal and X (C or N) elements, the properties of the MXenes can be tuned relatively easily by mixing and matching the terminating functional groups, as many theoretical studies have demonstrated[43,47]. A high spin-orbit coupling, which may be generated in a material by adding heavy elements, is the second requirement for a considerable DMI and even a strong magnetocrystalline anisotropy (MAE), which is, in turn, thought to be necessary for the presence of long-range magnetic order in 2D[50,51], The existence of early transition heavy metals like Hf, Ti, and Zr again makes MXenes a productive avenue for realizing skyrmions. Moreover, recent synthesis of chalcogen-decorated[52] and functionalized[42] and iodine-functionalized[42,53] MXenes have provided another novel route to introduce heavy elements like I and Te into the MXene structure. The proposed MXene space to be searched for strong DMI is illustrated in Fig. 1a. For simplicity, we examine only the materials with a single magnetic species containing metal layer on the top as determining the magnetic ground state of a 2D material with multiple magnetic species can be an extremely difficult task[54,55]. The possible magnetic species, M_{mag}, is chosen from $M_{mag} \in \{V, Cr, Mn\}$, all of which can be found in the known MAX phases, the precursor to MXenes. We explore MXenes possessing a total of 2, 3, and 4 metal layers, where the rest of the metal layers contain a single nonmagnetic species, M_{nonmag}. This species is chosen from the set $M_{nonmag} \in \{Sc, Ti, Y, Zr, Nb, Mo, Hf, Ta, W\}$. Some of these elements do not exist in known MAX phases yet, such as Y and W. Still, we include them in anticipation of future discovery, as lighter elements with similar electronic structures (Sc and Mo) are already found to exist in the MAX phases. The top and bottom terminating functional groups, T_{top} and T_{botom}, are chosen from the set T_{top}, $T_{botom} \in \{OH, O, F, Te, I\}$. The first three groups are found in known MXenes and usually originate from the etching solution[39]. The latter two elements, Te and I, have only recently been innovatively used as terminating functional groups[42,52,53], which provides an opportunity to insert heavy elements as terminating groups to boost the magnetic anisotropy and DMI effect. It should be noted that both $T_{top} \neq T_{botom}$ and $T_{top} = T_{botom}$ cases have been considered. As usual, $X \in \{C, N\}$, and a single X species is used for a particular material.

We also illustrate the concept of the nearest magnetic neighbors of these materials in Fig. 1b. MXenes with a single magnetic layer can be classified as a hexagonal or '6-6-6-12' magnetic material[55]. The top view of the magnetic layer is shown, and up to the 4th nearest magnetic neighbor of the central atom is shown using different colors. Different nearest-neighbor contributions are also highlighted, which we will explain in detail in the next section.

Using the criterion mentioned above, we end up with a total of 4050 materials: 1350 each for 2, 3, and 4 metal-layered MXenes.

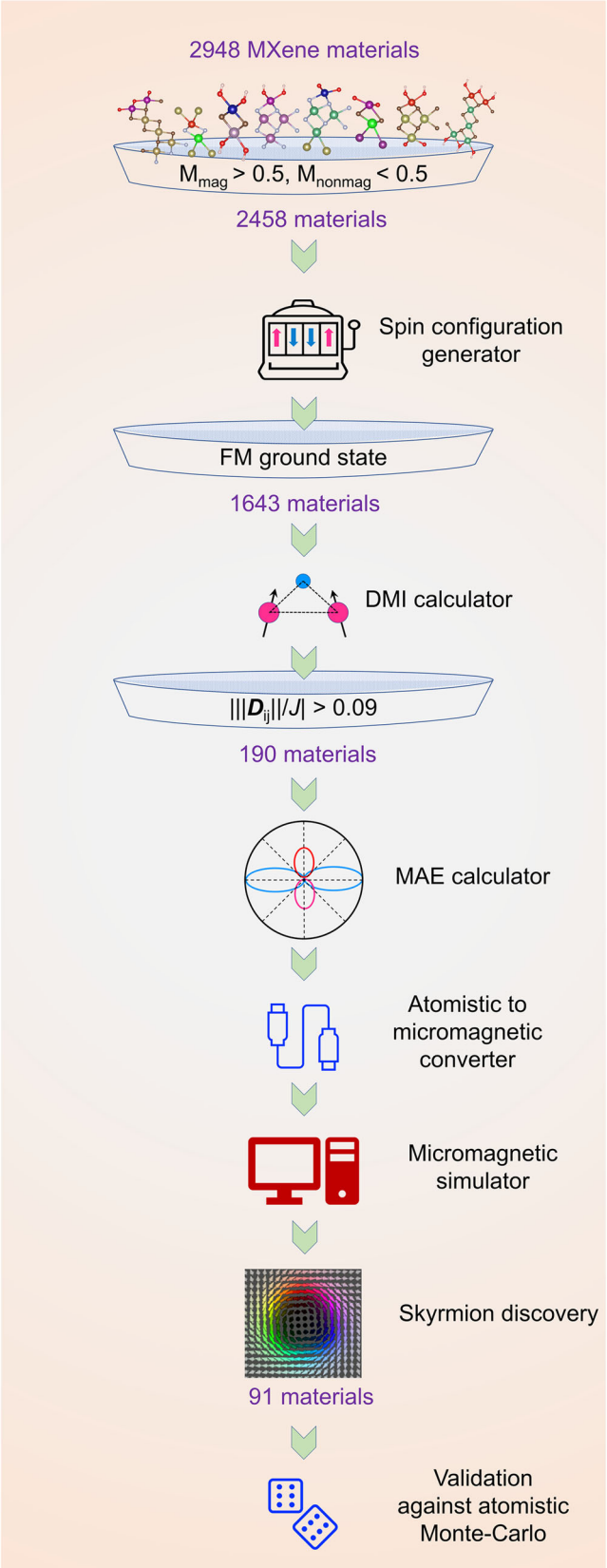

Fig. 2 The automated high-throughput workflow.

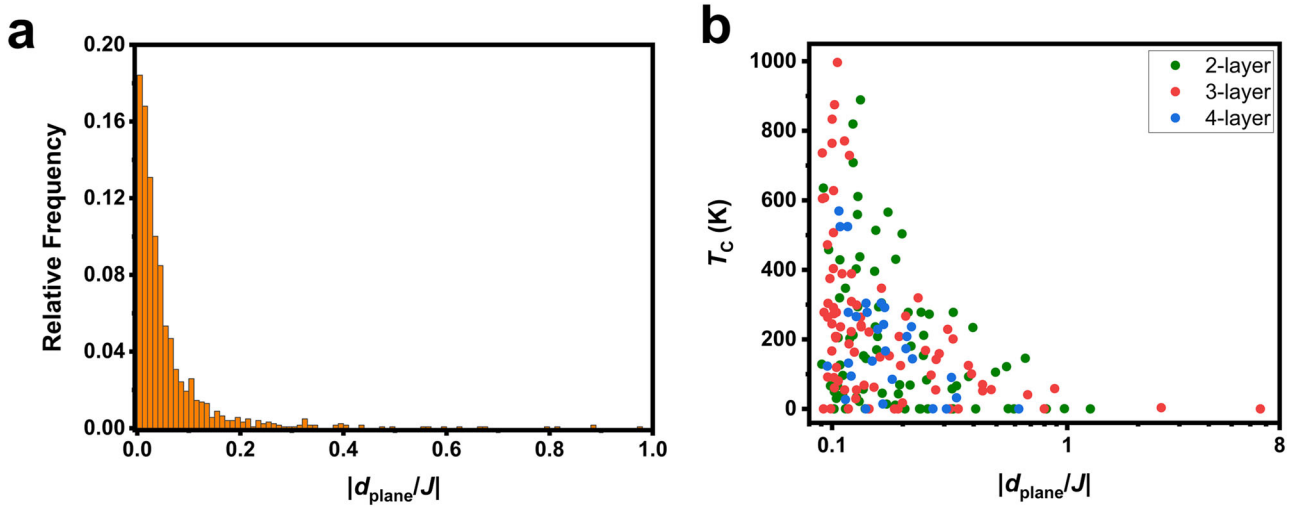

Fig. 3 Data distribution with respect to $|d_{plane}/J|$. a The distribution of the quantity $|d_{plane}/J|$ over the 1643 data points. **b** The distribution of T_c with respect to $|d_{plane}/J|$ for the 190 shortlisted materials after the ratio-based screening.

We subsequently randomly examine more than 70% of this vast material space using our high-throughput workflow.

High-throughput screening methodology

The designed high-throughput workflow is schematically depicted in Fig. 2. Density functional theory (DFT)-based calculations have been employed to determine the total energies and other relevant properties of the materials. It is, however, well known that the local or semi-local DFT, such as the one employing generalized gradient approximation (GGA) with exchange-correlation (XC) functional such as Perdew–Burke–Ernzenhof (PBE), suffers from high self-interaction error (SIE), especially for systems with localized *d* or *f* electrons which is the case for magnetic materials, resulting in highly erroneous predictions[56]. The classical way to tackle this has been the usage of on-site empirical corrections on the localized orbitals, such as Hubbard *U* and Hund *J* corrections (GGA + *U*). However, the value of these corrections can be extremely material specific[54,57]. Therefore, ideally, the *U* and *J* correction values should be recalculated for every material, which is obviously unsuitable for a high throughput study such as ours.

Recently developed meta-GGA XC functional SCAN (strongly constrained and appropriately normed)[58] is a semi-local density functional that fulfills all known constraints that the exact density functional must satisfy. It has been demonstrated that SCAN is superior to most gradient-corrected functionals and can even deal with strongly correlated magnetic materials without any empirical corrections[59–61]. However, SCAN is known to be vulnerable to numerical instabilities, and an upgraded version of this functional, r^{2}SCAN (regularized-restored strongly constrained and appropriately normed), has been introduced very recently and shown to match the accuracy of the parent SCAN functional but with much enhanced numerical efficiency with low-cost computational settings[62]. In our previous work, we have shown that an r^{2}SCAN-powered DFT-MC workflow can accurately predict the Curie temperature (T_C) of 2D magnets[55]. Other extensive benchmarking studies also find r^{2}SCAN to be an ideal XC functional for high-throughput materials discovery[63]. We thus identify r^{2}SCAN as the ideal XC functional for empirical-correction-free accurate DFT calculators, including the relaxation process, despite it being more computationally extensive than GGA + *U*.

The unit cell structure is first fully relaxed for each of the 2948 randomly chosen materials. Next, a static run is performed, and the formation energy is calculated. The formation energy of all the materials turned out to be reasonably negative, indicating good thermodynamic stability of these materials. Then a check is performed to see whether the supposed magnetic and non-magnetic layers of the material are genuinely magnetic and nonmagnetic. It is ensured that the magnetic moment of the magnetic species is >0.5 μ_B, whereas the magnetic moment of the nonmagnetic species is <0.5 μ_B, and there is a significant difference of magnetic moment between the two. After this, to search for the magnetic ground state, different possible symmetry-constrained spin configurations are generated (Supplementary Fig. 1), and their energies are calculated. In this work, we focus on the conventional skyrmions in ferromagnetic (FM) materials, albeit skyrmions can exist in antiferromagnetic (AFM) or ferrimagnetic (FEM) materials and can show some interesting properties[64,65]. Thus, materials exhibiting any other ground state than FM are discarded at this point. Next, the DMI strength of the materials is calculated using the well-established method of total energy difference of clockwise and anticlockwise spin canting with a periodicity of 4 sites[31,66]. We again note that our chosen materials exist in a hexagonal lattice, and for this lattice type applying Moriya's symmetry rules, the DMI interaction vector between site *i* and nearest neighboring site *j* can be expressed as $\boldsymbol{D_{ij}} = d_{plane}(\hat{\boldsymbol{u}}_{\boldsymbol{ij}} \times \hat{\boldsymbol{z}}) + d_z\hat{\boldsymbol{z}}$ where $\hat{\boldsymbol{u}}_{\boldsymbol{ij}}$ is the unit vector between sites *i* and *j*, $\hat{\boldsymbol{z}}$ is the unit vector normal to the plane, and d_{plane} and d_z are the in-plane and out-of-plane components of the DMI vector. However, for the hexagonal lattice, the sign of d_z changes in a staggered manner, averaging to a negligible effect of d_z on the total $\boldsymbol{D_{ij}}$[31,32]. Therefore, we only evaluate the values of d_{plane} while estimating the effect of DMI. We also follow the convention where a positive value of d_{plane} prefers clockwise spin canting, whereas a negative value would encourage anticlockwise spin canting.

After quantifying the DMI effect, we calculate the nearest neighbor exchange strength, *J*. The collinear total energies of spin configurations 0 (FM) and 1(AFM1) (see Supplementary Fig. 1) are fitted to the isotropic spin Hamiltonian:

$$H = -J\sum_{i>j} \boldsymbol{S}_i.\boldsymbol{S}_j \tag{1}$$

where $\boldsymbol{S}_i$ is the spin vector of the site in question, and $\boldsymbol{S}_j$ is the spin vector of the nearest neighbor. With a DMI term added, the value of which we have already determined, the Hamiltonian becomes:

$$H = -J\sum_{i>j} \boldsymbol{S}_i.\boldsymbol{S}_j - \sum_{i,j} \boldsymbol{D}_{ij}.(\boldsymbol{S}_i \times \boldsymbol{S}_j) \tag{2}$$

Note that to be consistent with our previous works[54,55], we express the spin vectors in a way that carries both a magnitude

and a direction. Another well-accepted convention is representing the spin values as unit vectors and accordingly scaling the values of the accompanying terms, such as J and $\boldsymbol{D}_{ij}$[31,32,67]. While comparing absolute values of these constants, they should be appropriately scaled according to the reported convention. At this point of our workflow, we impose perhaps the most important criteria for skyrmion formation, the absolute value of the $||\boldsymbol{D}_{ij}||/J$ ratio, which should be >0.1 for skyrmion formation[68]. To be on a safer side, we explore materials exhibiting $|d_{plane}\ /\ J| > 0.09$. This criterion filters out most of the materials, and we end up with only 190 materials, implying skyrmion-hosting materials are indeed quite rare even in our carefully curated search space that a priori tries to maximize the probability of finding such materials. The distribution of the quantity $|d_{plane}\ /\ J|$ over 1643 materials is shown in Fig. 3a, and it can be observed that the lion's share of materials possesses $|d_{plane}/\ J| < 0.09$.

It should be noted that we have used an isotropic Heisenberg Hamiltonian so far, which does not describe the complete picture for 2D magnets. The spin-orbit coupling (SOC)-included anisotropy calculations with the r^{2}SCAN functional, which must be fully self-consistent as dictated by implementation, are the most computationally expensive part of our pipeline[55]. We thus execute these calculations only for the potential 190 materials. We recalculate the total energies of all the spin configurations after orienting all the spins in the x and z directions. For a hexagonal lattice, it is difficult to orient the spins in the y direction, and therefore, we resort to an XXZ model with in-plane isotropy. This is usually a reasonable approximation for hexagonal 2D magnets because the in-plane anisotropy is usually much weaker than the out-of-plane anisotropy[69–71]. After all these, the data is fitted to the anisotropic Heisenberg Hamiltonian:

$$H = -J_1 \sum_{i>j} \boldsymbol{S}_i.\boldsymbol{S}_j - J_2 \sum_{i>k} \boldsymbol{S}_i.\boldsymbol{S}_k - J_3 \sum_{i>l} \boldsymbol{S}_i.\boldsymbol{S}_l - K_{1z} \sum_{i>j} S_i^z S_j^z - K_{2z} \sum_{i>k} S_i^z S_k^z$$
$$-K_{3z} \sum_{i>l} S_i^z S_l^z - A_z \sum_i (S_i^z)^2 - \sum_{i>j} \boldsymbol{D}_{ij}.(\boldsymbol{S}_i \times \boldsymbol{S}_j) - 2\mu_B \sum_i \boldsymbol{B}.\boldsymbol{S}_i \quad (3)$$

Here, J_1, J_2, and J_3 represent isotropic exchanges between the 1st, 2nd, and 3rd nearest magnetic neighbors, respectively. $\boldsymbol{S}_i$ represents the spin of the site in question, and $\boldsymbol{Sj}$, $\boldsymbol{S}_k$, and $\boldsymbol{S}_l$ are the spins of sites at the 1st, 2nd, and 3rd nearest magnetic neighbor shells. These spins are all three-dimensional vectors, and the individual spin components in the z direction are represented as S_n^z, where $n = i, j, k$. The value of the electron g-factor (gyromagnetic factor) is assumed to be 2. We again emphasize that the magnitude of spins is not necessarily unity as per our chosen convention, but half (division by the g-factor) of the total magnetic moment (expressed in μ_B) of the unit cell with a single magnetic atom. The K_{pz} terms represent the anisotropic exchange for neighbor shell p ($p = 1, 2, 3$) in the z-direction. The A_z term represents the out-of-plane single-ion anisotropy, the $\boldsymbol{B}$ term signifies the applied magnetic field, and μ_B is the Bohr magnetron. The assumption of $g = 2$ leads to the prefactor of 2 in the last (Zeeman) term. Since we generate a total of 4 different spin configurations, we can find out the isotropic and anisotropic exchange terms till the 3rd nearest neighbor. However, the exchange strength usually goes down by at least an order after the first nearest neighbor, which can be confirmed from Supplementary Data. This is also expected for the DMI interaction, and as the DMI strength is usually much weaker than the isotropic exchange, its beyond first-nearest-neighbor interactions are deemed negligible[66]. Moreover, the computational cost of determining the DMI interactions with multiple neighbor shells is enormous, as they also require SOC-included, fully self-consistent calculations with constrained magnetic moments for much larger supercells[72]. The different neighbor-dependent terms in the context of the hexagonal lattice are illustrated in Fig. 1b.

Next, we convert the atomistic energetics to micromagnetic parameters. Micromagnetic simulations have recently become the de-facto tool to simulate noncollinear structure-based devices[30,31,33,73]. The primary reason is that the large size of the noncollinear magnetic structures is often prohibitively costly to simulate atomistically. Moreover, the atomistic Heisenberg Hamiltonian is best suited to insulators and large-bandgap semiconductors, as it assumes high localization of spins, which is clearly not the case for metallic materials. Most of our examined MXene materials are metallic by nature, and the Heisenberg Hamiltonian is often used as a first-order approximation to predict the properties of metallic materials[31,32,54,74,75]. In our previous work, we have shown that the Heisenberg Hamiltonian-based DFT-MC framework consistently underpredicts the Curie temperature for metallic 2H (experimental 430 K, predicted 332 K) and 1 T (experimental >300 K, predicted 280 K) VSe_2, but somewhat captures their high-Curie point nature[55]. However, the micromagnetic theory is expected to provide a much more realistic prediction for metallic FM materials. Based on these reasons, we select micromagnetic simulations as the ideal tool for finding skyrmions in our shortlisted materials. We have also tried to validate the micromagnetic predictions using atomistic Heisenberg Hamiltonian-based MC simulations for a few cases.

We have also predicted the Curie temperature of the shortlisted 190 materials using the Heisenberg model-based MC simulations, similar to our previous work[55]. As mentioned before, this method can underpredict the T_C for metallic materials but provides a good qualitative idea about whether the material can exhibit a high Curie point. The distribution of T_C of the 190 materials with respect to our main figure of merit $|d_{plane}\ /\ J|$ is plotted in Fig. 3b, and it can be observed that materials with high T_C are quite improbable to have large $|d_{plane}\ /\ J|$, i.e., probability of skyrmion formation. A few outliers, however, can show extremely high $|d_{plane}\ /\ J|$, but near-zero T_C because of their feeble J values.

Discovery of skyrmions and their characterization

After micromagnetic theory-based energy minimization, the magnetic state with no external magnetic field ($T = 0$, $B = 0$) is visually depicted in the Supplementary Repository for all 190 shortlisted materials. Most materials exhibit worm-like domains, which are clear evidence of a strong DMI effect. A few materials (out-of-plane: eight 2-layer, ten 3-layer, three 4-layer, in-plane: six 2-layer, five 3-layer, one 4-layer) end up with a clean ferromagnetic state after the minimization, which is indicative of the fact that the symmetric exchange is stronger compared to the DMI in these materials, and skyrmions are highly unlikely to form. For a few materials (out-of-plane: eight 2-layer, seven 3-layer, four 4-layer, in-plane: two 2-layer, one 3-layer, one 4-layer), however, stabilized skyrmions can be observed even at $B = 0$. Based on visual observations, we shortlist 91 materials (78 out-of-plane, 13 in-plane) that can host stable skyrmions. These include materials exhibiting domains as well as stable skyrmions after energy minimization. The materials exhibiting domains at $B = 0$ can potentially be hosts of stable skyrmions with the application of a suitable finite magnetic field, as demonstrated by several previous studies[32,33].

Among the shortlisted 78 out-of-plane 2D FM Mxenes, 20 materials can host spontaneous stable skyrmions without any externally applied magnetic field. In terms of technological application, these materials are highly desirable, as they omit the requirement of bulky electromagnets in the device and can be incorporated with the existing integrated circuit (IC)-based technologies, allowing for smaller and dense devices. State-of-the-art ICs, however, reliably work at room temperature and beyond. This will also be the requirement for skyrmion-based

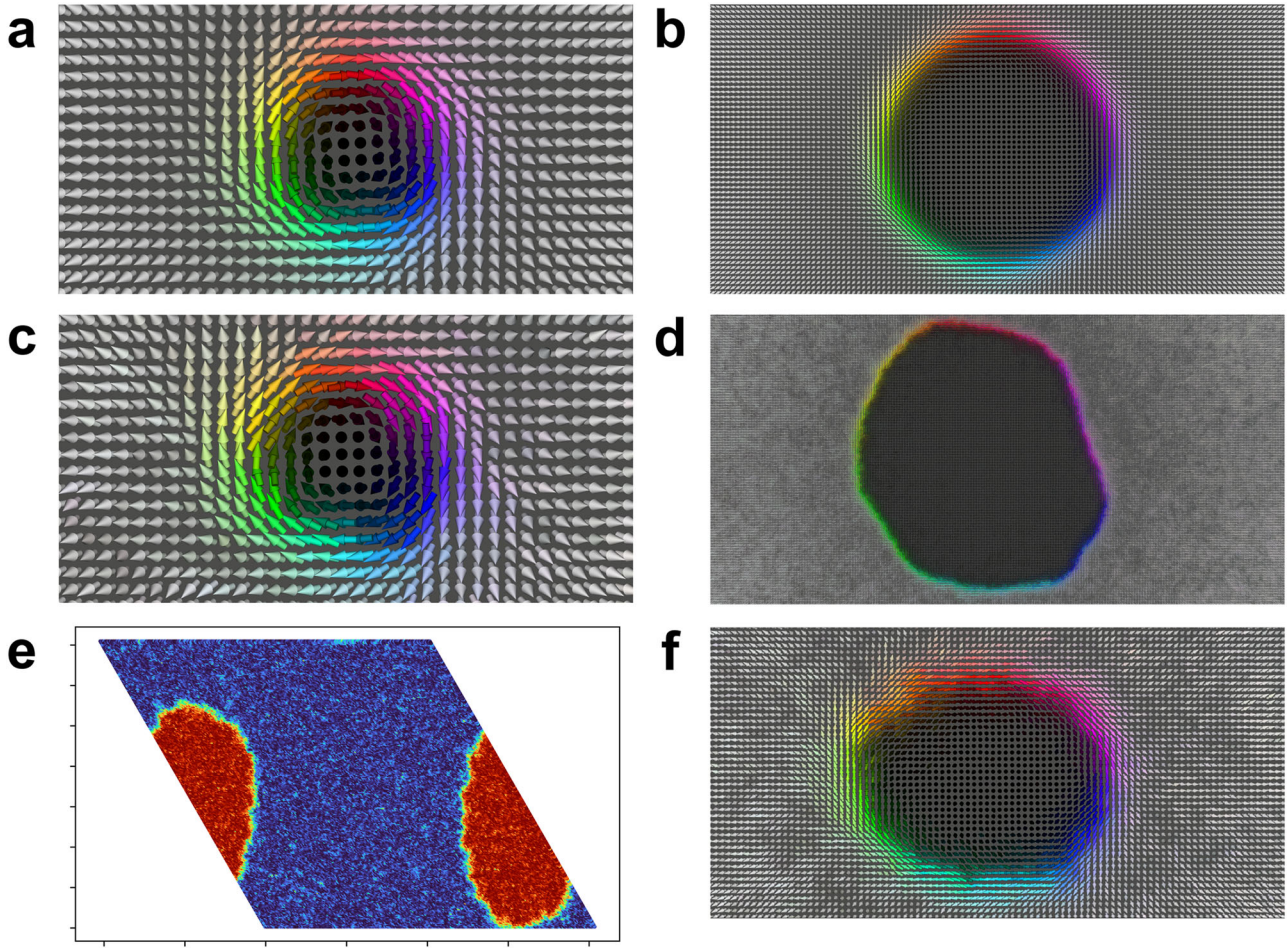

Fig. 4 Out-of-plane 'unipolar' skyrmions. Skyrmions with no external field in the materials (**a**) CrW_3C_3II and (**b**) CrW_3C_3IF after micromagnetic energy minimization. The same skyrmions after exposure to 300 K temperature for 1 ns in (**c**) CrW_3C_3II and (**d**) CrW_3C_3IF as predicted by micromagnetic simulations. **e** Skyrmion in CrW_3C_3II at 285 K and zero field as predicted by atomistic Monte Carlo simulation. **f** Micromagnetic simulations predicted skyrmion in CrW_3C_3IF at 300 K and 0.5 T applied field after 1 ns. The 'Mumax3' color scheme has been used for all micromagnetic-simulated results, and the 'Turbo' color scheme has been used for all atomistically simulated results. Only the *z* component of the spin vector is plotted in real space in **e**. However, all three (*x*, *y*, and *z*) components of the spin vector are plotted in Supplementary Fig. 2.

technology if they merge with the current technology. The T_C is a good predictor of high-temperature skyrmion stability, albeit the critical temperature at which the skyrmions remain stable is usually far below the T_C[32]. As depicted in Fig. 3a, materials with potential high-temperature skyrmions are indeed quite rare. We focus on two 4-layer materials with mostly similar compositions but contrasting properties: CrW_3C_3II and CrW_3C_3IF, with Curie points >524 K in anticipation of room-temperature skyrmions. Their energy-minimized magnetic states are shown in Figs. 4a and 4b, respectively. The skyrmion diameter of these materials turns out to be about 24 nm and 64 nm.

Next, we expose these two different-sized skyrmions to 300 K temperature with the means of micromagnetic simulation for 1 ns. The skyrmion hosted in CrW_3C_3II exhibits minimal changes after spending 1 ns at room temperature, but the skyrmion hosted in CrW_3C_3IF starts to spread out as soon as the temperature is applied and ends up with a gigantic core region after 1 ns, suggesting leaving it at room temperature for a long time might turn it into a domain-structure. These two states are shown in Fig. 4c, d. As mentioned before, an external magnetic field is a convenient way to tune the shape and size of skyrmions. With a moderate field of $B = 0.5$ T in the out-of-plane direction, the skyrmion diameter in CrW_3C_3IF reduces to about 50 nm after minimization. When the state is exposed to room temperature for 1 ns, it does undergo some visually noticeable shape changes, i.e., it becomes rather oval-shaped, deviating from its original round nature, but the skyrmion core and boundary regions hold on to their structural integrity quite well. They do not show any signs of spreading with advancing timesteps at all. This magnetic state is depicted in Fig. 4f.

We also try full atomistic MC simulations based on the previously mentioned anisotropic Heisenberg Hamiltonian for the material CrW_3C_3II. While using a highly parallel GPU (graphical processing unit)-accelerated micromagnetic simulator[76], we can simulate a large 512×512 nm cell in a matter of minutes, the Metropolis algorithm-based atomistic MC gets serially executed on a CPU (central processing unit) core, and the largest cell we could simulate was 82×82 nm, which takes around 11 h for a set of parameters. Moreover, the cell in the simulation should be large enough to avoid spurious interactions from its periodic images. With these constraints, the magnetic state of CrW_3C_3II turns out to be reliably manageable for atomistic MC because of the smaller skyrmion size. Starting from the same random state, we see that a spontaneous skyrmion forms in CrW_3C_3II up to 285 K, with the skyrmion size roughly matching the micromagnetic prediction. This state is depicted in Fig. 4e. At 300 K and $B = 0$, however, our MC simulations consistently predict domain states. A mismatch between the micromagnetic and atomistic theory is expected for reasons mentioned before, and possible a manifestation is observed here. With a mild external field $B = 0.2$ T in the vertical

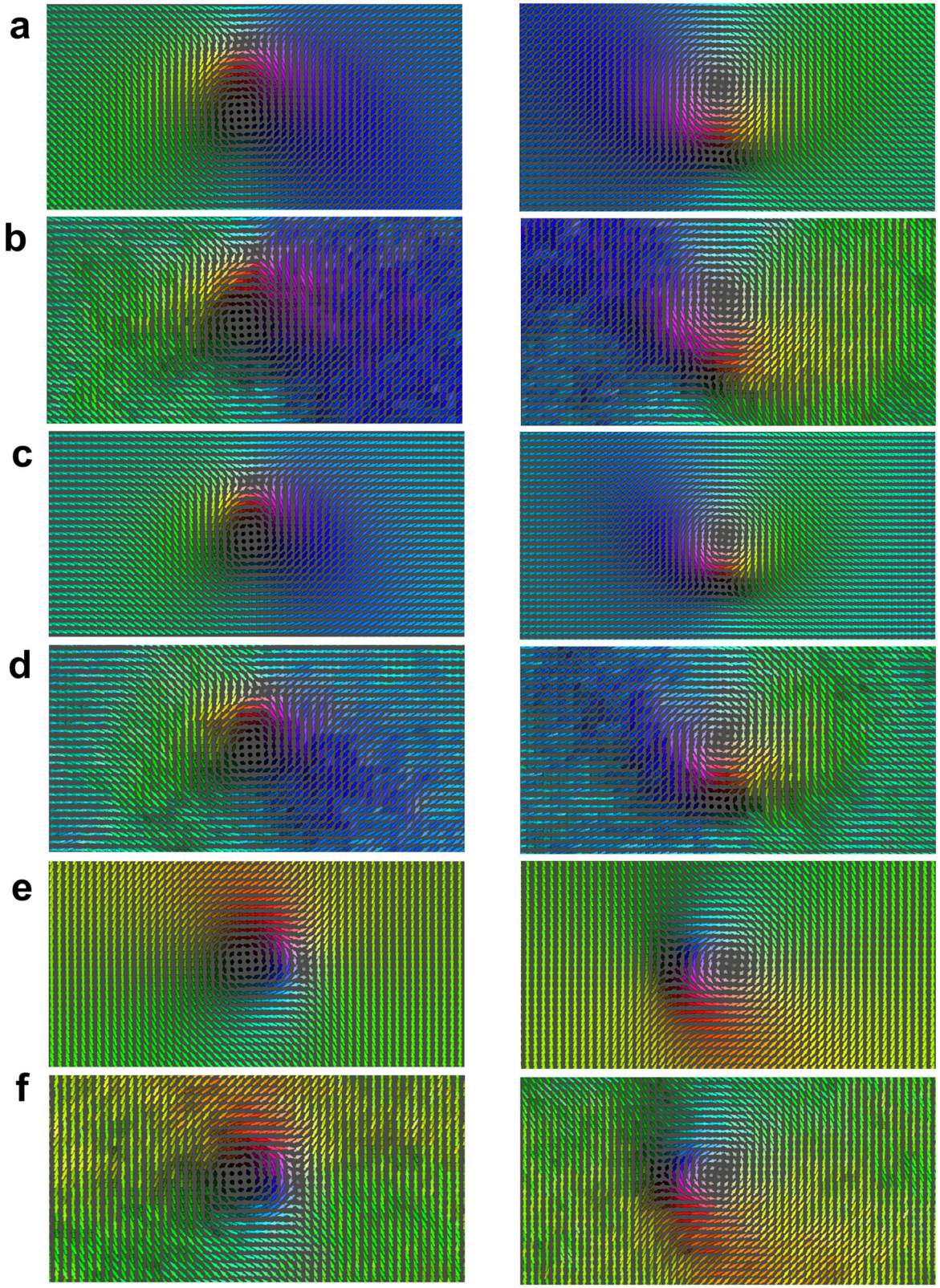

Fig. 5 In-plane 'bipolar' skyrmions. The bipolar skyrmions in $MnHf_2C_2IF$ without any external field after (**a**) energy minimization and (**b**) spending 1 ns at 200 K as predicted by micromagnetic simulations. The skyrmions in the same material with a 0.25 T applied field in the *-x* direction after (**c**) energy minimization and (**d**) exposure to 200 K temperature for 1 ns. The skyrmions with a 0.25 T applied field in the *y* direction after (**e**) energy minimization and (**f**) spending 1 ns at 200 K.

direction, however, the skyrmion can be stabilized at room temperature, albeit with a slightly smaller size. All the different atomistic MC results are shown in detail in Supplementary Fig. 2. This exercise validates the prediction of micromagnetic simulations through atomistic MC simulations.

Next, we focus on the exotic in-plane skyrmions. As discussed before, the specialty of skyrmions in in-plane magnets is that they can be bipolar in nature, i.e., skyrmions with two different polarities of topological charges can coexist in the material, increasing their ability to pack more information than their out-of-plane counterparts. In-plane skyrmions are extremely rare and, to the best of our knowledge, have not been reported for any 2D material yet. We find only 13 materials capable of hosting in-plane skyrmions. Among these, we focus on the 3-layer MXene $MnHf_2C_2IF$, which is predicted to host spontaneous bipolar skyrmions and a high Tc of around 299 K. The bipolar skyrmions in the energy-minimized magnetic state are highlighted in Fig. 5a. The noncollinear magnetic structure is somewhat similar but subtly different from the previous theoretical prediction[30]. The skyrmions are quite large in size, measuring around 113 nm in diameter each. Moreover, bringing the two skyrmions of opposite polarity closer than about 150 nm (distance between the centers) destroys both after energy minimization, leaving behind a clean ferromagnetic state. The large size of these skyrmions might undermine their information packing density. However, as mentioned earlier, the application of an external magnetic field is an efficient way of controlling the size of the skyrmions, which we will explore next.

As the critical temperature for skyrmion existence is usually relatively lower than the material's Curie point, to test the thermal stability of the bipolar skyrmions, we expose them to 200 K temperature for 1 ns employing micromagnetic simulations. The results are illustrated in Fig. 5b and Supplementary Fig. 3. The skyrmion cores tolerate the temperature well, but the ferromagnetic background of the material gets quite perturbed, making it challenging to identify the skyrmions. Clearly, the large size of the quasiparticles plays a role in this.

Next, we apply a mild field of $B = 0.25$ T in the direction of the ferromagnetic background (-x) to observe its effect on the skyrmion size and stability. After energy minimization, the skyrmion size reduces highly to around 50 nm each, making the system much more suitable for high-density memory applications. These skyrmions are depicted in Fig. 5c. Moreover, the whole system tolerates the 200 K temperature well. The skyrmions and the entire magnetic state after being exposed to 200 K temperature for 1 ns are illustrated in Fig. 5d and Supplementary Fig. 4. The ferromagnetic background keeps its uniform nature much better than the no-field case, and it becomes much easier to identify the smaller skyrmions on this background.

We also experiment with magnetic fields oriented in the y direction, perpendicular to the magnetic direction of the ferromagnetic background. The energy-minimized bipolar skyrmions and the magnetic state are depicted in Fig. 5e and Supplementary Fig. 5 for this case. The ferromagnetic background fully aligns with the direction of the applied field, as an in-plane isotropy has been imposed on the system, as discussed before. The skyrmion size becomes even smaller, around 37 nm in diameter. The bipolar skyrmions and the magnetic state are illustrated in Fig. 5f and Supplementary Fig. 5 after the system being exposed to 200 K temperature for 1 ns. Again, the micromagnetic simulations predict a much better outcome regarding the integrity of the ferromagnetic background and skyrmion stability. The in-plane skyrmions, therefore, should be highly susceptible to external magnetic fields, and the skyrmion size and stability can be well-controlled by this method.

We then attempted to simulate the in-plane skyrmion state of $MnHf_2C_2IF$ using an atomistic MC process in an 82×82 nm cell, which is the largest cell we can simulate. Interestingly, unlike the out-of-plane case, when starting from a random spin configuration, the system always ends up with worm-like domain states instead of a skyrmion state. It appears the choice of the initial state is crucial to stabilize the in-plane skyrmions, which was also true in the case of micromagnetic simulations. We used the recipe of Moon et al.[30] to stabilize the in-plane skyrmion with micromagnetic simulations. This involves creating an initial state with out-of-plane Néel skyrmions with suitable topological charges and then revolving all spins by either 90° or −90°, depending on the skyrmion charge. We use the same idea here and extract the out-of-plane skyrmion state of CrW_3C_3II at 285 K (shown in Fig. 4e) and rotate all spins of the state such that the all the spins of the ferromagnetic background align to the y-axis. This is because the skyrmion of the initial state seems quite elongated in the y direction, and according to the micromagnetic simulations, the spins of the ferromagnetic state should be aligned to the y direction to host this skyrmion properly. The initial state and the MC-deduced final states for temperatures 1 K, 2 K, 5 K, 15 K, 25 K, and 40 K are plotted in Supplementary Fig. 6. At lower temperatures, such as 1 K, 2 K, and 5 K, the MC-evaluated skyrmion structure can be observed quite clearly. Various features of the in-plane skyrmion obtained from the micromagnetic simulations are reproduced, such as the symmetric $+x$ and $-x$ aligned edges along the elongated (y) direction, asymmetric $+z$ (localized dot-like) and -z (delocalized line-like) aligned edges along the shortened (x) direction, and the -y aligned skyrmion core. Especially, the tiny but intense red ($+z$ aligned) and blue spots ($-$z aligned) in the m_z plots reveal spin vectors that are completely out-of-the-plane, which are important characteristics of the in-plane skyrmion. However, at the temperature of 40 K, the skyrmion structure gets quite perturbed and looks to be on the verge of being destroyed. This prediction is quite different from the micromagnetics-predicted skyrmion stability at 200 K. As mentioned before, like most MXenes, the $MnHf_2C_2IF$ is also metallic in nature, and the localized Heisenberg model can only be used as somewhat of a first-order approximation in this case for obvious reasons. The underestimation of temperature for a stable magnetic order of in-plane 2D magnets is somewhat consistent with our previous work, where the Heisenberg Hamiltonian-based DFT(r^2SCAN)-MC framework underpredicts the Curie temperature for metallic 2H (experimental 430 K, predicted 332 K) and 1 T (experimental >300 K, predicted 280 K) VSe_2[55]. Apart from being orders of magnitude faster, accuracy is one of the main reasons why micromagnetic simulation, which is expected to be more accurate in terms of experimental observations for metallic materials, is used as the main screening tool, and not the Heisenberg model-based DFT-MC framework. However, the atomistic MC results can provide qualitative validation of the micromagnetics-predicted results, which can act as a useful sanity check.

DISCUSSION

Theoretically, the MXene structures can be functionalized using any suitable functional groups. Previous computational studies have predicted properties of MXene decorated with various functional groups such as H, O, F, Cl, Br, OH, NO, CN, PO, OBr, OCl, SCN, NCS, and OCN[43]. Furthermore, innovative functionalization with heavy elements such as Se, Br, Sb, Te and I expands the MXene space even further[42,52,53]. Recent experimental realization of MBenes[77–79], where the species X of MXenes gets substituted with the element Boron, has opened another horizon of similar materials. In this work, we have only explored a small fraction of this enormous material space due to the computational limitations, but with the rapid advancement of computer hardware as well as software, we are hopeful that building on the methodology developed in this work most of the MXene/MBene space can

be explored in the near future to find excellent skyrmion-hosting materials.

The formation energy is considered the metric for the thermodynamic stability of a material but is only part of the full stability picture. A full phonon spectrum must be calculated to examine a material's dynamic stability. However, calculating a full phonon spectrum of the materials examined in this work, especially using the r^{2}SCAN meta-GGA functional, is prohibitively costly. However, we were able to calculate the phonon frequencies at the zone center (Γ-point) for the three focused materials: CrW_3C_3II, CrW_3C_3IF, and $MnHf_2C_2IF$. All these materials show negligible imaginary frequencies at the Γ point (see Supplementary Table 1), indicating good dynamical stability. The absence of imaginary modes at the zone center or other symmetry points is usually considered an indication of the dynamic stability of a material when a calculation of the full phonon spectrum is not possible[44,45,80]. The electronic density of states (DOS) of these three materials is also plotted in Supplementary Fig. 7 along with the projected DOS contribution from the *d* band of the magnetic species. All three materials turn out to be metallic with highly asymmetric contribution from the up and down spin channels at the Fermi level, reflecting the ferromagnetic state of the material.

We note that there could be multiple origins for the DMI interaction in a magnetic material. In the case of band magnetism for metals, especially for the case of Co/Pt (111) it was found that the DMI is strongly dependent on the angle between magnetic moments[81]. For these cases, the method of total energy difference of clockwise and anticlockwise spin canting with a periodicity of 4 sites might overestimate the value of the DMI interaction, and a detailed study of DMI dependence on spin rotation is required for an accurate elucidation of the phenomenon. This is out of the scope of a high-throughput study such as ours, but more materials-focused studies might want to consider performing this investigation for more detailed insights and accurate description of the DMI.

To summarize, we develop a high-throughput automated workflow in this work that rapidly scans a carefully curated large MXene space to find materials capable of hosting typical unipolar and exotic bipolar skyrmions. In fact, by exploiting the in-plane magnetism of the chosen 2D magnets, we stabilize the rare bipolar skyrmions, which is otherwise extremely challenging to realize in typical bulk materials. Since we use a high-fidelity XC functional, we expect our theoretical prediction to be in good agreement with any future experimental efforts. Several promising materials have been identified that can host room-temperature classical skyrmions or bipolar in-plane skyrmions. Our work might accelerate the development of fully 2D materials-based skyrmion-operated logic and memory devices.

METHODS

DFT calculations

DFT calculations of this work are carried out using a meta-generalized gradient approximation (meta-GGA) as implemented in the code Vienna Ab initio Simulation Package (VASP)[82–85] with the Projector-Augmented-Wave (PAW)[86] method using the r^{2}SCAN exchange-correlation functional[62]. The Materials Project[87] recommended pseudopotentials (https://docs.materialsproject.org/methodology/mof-methodology/calculation-parameters/psuedopotentials) have been used throughout. A sufficiently large cutoff energy of 520 eV is used to avoid Pulay stress. A Γ-centered k-points grid with reciprocal density 72 Å^{-3} is used to sample the Brillouin zone (BZ) for all structural relaxations. A similar *k*-mesh with reciprocal density 300 Å^{-3} is employed for all static runs, including the non-collinear ones. Electronic convergence is set to be attained when the difference in energy of successive electronic steps becomes less than 10^{-6} eV, whereas the structural geometry is optimized until the maximum Hellmann-Feynman force on every atom falls below 0.02 eV/Å. A large vacuum space of 25 Å in the vertical direction is applied to avoid any spurious interaction between the periodic images. All crystal structures are visualized using the tool VESTA[88].

All the materials we explore are non-centrosymmetric in the vertical direction, and therefore, appropriate dipole correction in this direction is essential for the accurate prediction of total energies and other properties. For all relaxations, we apply the dipole correction in the *z*-direction. However, we choose not to use the dipole correction for the static runs. Despite numerous attempts with different settings, performing static runs, especially the noncollinear ones with dipole correction and the r^{2}SCAN functional, do not appear to converge. However, with the reasonable assumption that the dipole correction does not depend on the spin orientations, they can be absorbed into the Hamiltonian's spin-independent energy term (E_0) and safely omitted for the static runs. The obtained magnetic parameters are independent of the E_0 term and, in turn, the dipole corrections. Similarly, the DMI term determination also involves subtracting the total energies of two spin spirals, and the spin orientation-independent dipole correction should cancel out as well. However, this is not the case for geometry optimization, and thus the optimizations have been performed including the dipole corrections to the total energies and forces for accurate predictions.

The phonon calculations are done using a finite difference approach (IBRION = 6). The unit cell and a $19 \times 19 \times 1$ Γ-centered *k*-points sampling are used, and each atom is displaced +0.015 Å and −0.015 Å along each cartesian direction for these calculations.

In a previous work of ours[47], we have shown that for 2-layer MXenes, the inclusion of Van der Walls (vdW) corrections introduces negligible changes in the structures. However, in this work, we have explored MXenes with up to 4 metal layers. For the three focused materials, CrW_3C_3IF, CrW_3C_3II, and $MnHf_2C_2IF$, containing 4 and 3 metal layers, we examine the effect of nonlocal vdW correction for completeness. We use the r^{2}SCAN + rVV10 vdW density functional parameterized by Ning et al.[89], which is demonstrated to provide an accurate estimation of various physical and chemical properties for a variety of materials, including bulk and layered materials. Somewhat expectedly, we find that the reduction of the lattice parameter and thickness due to the introduction of the vdW correction is negligible (0.22 and 0.03% for CrW_3C_3IF, 0.24 and 0.09% for CrW_3C_3II, 0.29 and 0.03% for $MnHf_2C_2IF$) for all three materials, supporting our choice of not including the expensive vdW corrections for all calculations.

The enormous computational challenge involving the r^{2}SCAN functional was managed by executing the VASP code in the PARAM-Siddhi-AI supercomputer (https://en.m.wikipedia.org/wiki/PARAM) containing state-of-the-art NVIDIA A100 GPUs. 8 such GPUs and 24–96 CPU cores have been used to process each material.

Automation of high-throughput workflow

A simple python library, pymag2D, was written to modularize various operations of the automated workflow, and python scripts were written using this library to scan the materials space in an automated manner. The python libraries pymatgen (Python Materials Genomics) and custodian[90] have been used extensively in the high-throughput pipeline code to achieve full automation. The library Atomic Simulation Environment (ASE)[91] has also been used for some operations. The automated workflow uses the MagneticStructureEnumerator class from pymatgen.analysis.magnetism.analyzer module to generate the different spin configurations. The same protocol from our previous work has been used here for relaxation and static runs of various spin configurations[55]. The site-resolved magnetic moments are taken directly from the

VASP OUTCAR files for the magnetic moment-based initial screenings. However, the spin values are obtained from the OSZICAR files. The total magnetic moment of the cell for the FM configuration is collected, and then the quantity is divided by (2 × the number of magnetic atoms in the cell) to obtain the S value[55].

DMI calculations

The DMI strength of the materials is calculated using the well-established method of total energy difference of clockwise and anticlockwise spin canting with a periodicity of 4 sites, i.e., using 4 × 1 supercells[31,32,66]. The in-plane DMI component, d_{plane} has been derived as $d_{plane} = \frac{E_{CW} - E_{ACW}}{12S^2}$ where E_{CW} and E_{ACW} are the total energies of the clockwise and anticlockwise canted spin configurations, and S is the magnitude of the spin for a magnetic site. The total energies are determined using noncollinear DFT with the SOC effect included and the constrained magnetic moment approach. The direction of the magnetic moments is constrained with a penalty weight (LAMBDA) of 50. The energy arising from the penalty functional always remains below 5 μeV/supercell and is almost the same for the CW and ACW cases, and therefore mostly cancels themselves out. The same can be said about dipole corrections, assuming it is mostly spin orientation-independent.

The value of the d_z component can be estimated[32,92] using the simple relation $d_z = d_{plane}/tan(\theta_{ij})$ where θ_{ij} is the average of M_{mag}-T_{top}-M_{mag} and M_{mag}-X-M_{mag} tilting angles, assuming most of the superexchange between the neighboring M_{mag} sites occurs through the nearest T_{top} and X atoms. In this work, however, we have neglected the contribution of d_z as collectively their contributions vanish in the hexagonal lattice.

Calculation of micromagnetic parameters

The magnetic anisotropy energy term (K_u) is calculated as the total energy difference per unit volume with the magnetic moments oriented in-plane and out-of-plane. Similarly, the saturation magnetism (M_{sat}) is calculated as the total magnetic moment per unit volume. The micromagnetic DMI constant (D) is calculated as $D = \frac{\sqrt{3}d_{plane}}{at}$ where a is the lattice parameter of the MXene and t is the thickness of the atomic magnetic layer[31,66]. The exchange stiffness A is calculated as $A = \frac{U}{V(|\boldsymbol{M}|^2)}$ where V is the volume of the unit cell and M is the magnetic unit vector. The exchange energy U defined as the difference between the average total energy of noncollinear clockwise and anticlockwise spin-canted structures, and the total energy of the collinear spin configuration[18,31].

Determining the thickness of the single atomic layer of the magnetic species can be tricky. To obtain this, the atomic Bader volume ($V_{atom\text{-}bader}$) of the magnetic species is first determined. This is done using the Bader partitioning code developed by the Henkelman group[93–95]. Then the atomic radius of the magnetic atom ($r_{atom\text{-}bader}$) is determined assuming the magnetic atom is perfectly spherical, i.e., $\frac{4}{3}\pi r^3_{atom-bader} = V_{atom-bader}$. Finally, the thickness of the atomic layer is determined as $t = 2r_{atom\text{-}bader}$. Similarly, the thickness of the unit cell is determined by taking into account the $r_{atom\text{-}bader}$ of the terminal atoms along the vertical direction, which is ultimately used to calculate unit cell volume V. The skyrmion diameters are measured using the process of Yuan et al.[31], assuming a 3% fall in the magnetism marks the beginning of the skyrmion edge.

Micromagnetic simulations

All the micromagnetic simulations are performed using the GPU-accelerated code Mumax3[76]. All simulations are performed in 512 × 512 nm periodic cells, with cell size 1 × 1 nm and periodic boundary conditions applied along the in-plane directions. The magnetic states are initialized with appropriate Néel skyrmions (single unipolar or dual bipolar), and then an energy minimization was performed using the 'Relax()' command. A large Landau-Lifshitz damping constant $\alpha = 1$ was employed to accelerate the finite-temperature simulations[51].

In the case of in-plane magnetism, to properly implement the in-plane isotropic XXZ model, a negative value of anisotropy constant (K_u) is used with the anisotropy explicitly mentioned to be in the vertical direction (AnisU = vector(0,0,1)). This behavior energetically encourages the spins to orient in the plane without a specific preference for an in-plane direction. Conversely, a positive K_u with the same anisotropy direction settings properly simulates the XXZ model for a material with an out-of-plane magnetic moment.

All micromagnetic visualizations have been performed with the mumax-view website (https://mumax.ugent.be/mumax-view/) or the mumax-convert tool included with Mumax3.

MC simulations

MC simulations of the above-mentioned Hamiltonian (Eq. (3)) have been performed using the Metropolis algorithm with the single-spin update scheme. To validate the micromagnetic simulations, a 250 × 250 supercell (around 82 × 82 nm) with in-plane periodic boundary conditions containing 62500 magnetic sites has been used to simulate the 2D systems, minimizing the size effects. In total, 2×10^5 Monte Carlo steps (MCS) have been performed for each set of parameters[32–34]. For the T_C calculations, however, smaller 64 × 64 supercells with 4096 sites have been used, and the total magnetism and susceptibility are calculated as the average over the last 10^5 MCS for each temperature, similar to our previous work[55].

DATA AVAILABILITY

The authors declare that the primary data supporting the findings of this study are available within the paper and its supplementary files. The online Supplementary Repository can be freely accessed at https://doi.org/10.6084/m9.figshare.22153955.v2. The magnetic parameters of the 190 shortlisted materials can be found as Supplementary Data with this paper. A brief guide on how to read the data is available as Supplementary Note 1 in the Supplementary Information file. The images of magnetic states after energy minimization with the means of micromagnetic theory can be found in the files 'mag_states_all.zip' and 'mag_states_shortlisted.zip' of the Supplementary Repository. Moreover, relaxed crystal structures of all materials examined in this work are available here. Other relevant data are available from the corresponding author upon reasonable request.

CODE AVAILABILITY

All the relevant custom codes can be found at https://doi.org/10.6084/m9.figshare.22153955.v2 in the zip file named 'codes.zip' and the GitHub repository https://github.com/arnabkabiraj/pymag2d. The details about VASP, a proprietary code, can be found at https://www.vasp.at/. The open-source code Mumax3 is available at http://mumax.github.io/.

Received: 15 March 2023; Accepted: 14 September 2023;
Published online: 25 September 2023

REFERENCES

1. Vakili, H. et al. Skyrmionics—computing and memory technologies based on topological excitations in magnets. *J. Appl. Phys.* **130**, 070908 (2021).
2. Kiselev, N. S., Bogdanov, A. N., Schäfer, R. & Rößler, U. K. Chiral skyrmions in thin magnetic films: new objects for magnetic storage technologies? *J. Phys. Appl. Phys.* **44**, 392001 (2011).
3. Lee, M.-K. & Mochizuki, M. Reservoir computing with spin waves in a skyrmion crystal. *Phys. Rev. Appl.* **18**, 014074 (2022).
4. Raab, K. et al. Brownian reservoir computing realized using geometrically confined skyrmions. *Nat. Commun.* **13**, 6982 (2022).
5. Zhang, Z. et al. Ultra-low-power reservoir computing based on synthetic antiferromagnetic skyrmion pairs. *IEEE Electron Device Lett.* **43**, 1567–1570 (2022).
6. Jiang, W. et al. Physical reservoir computing using magnetic skyrmion memristor and spin torque nano-oscillator. *Appl. Phys. Lett.* **115**, 192403 (2019).

7. Prychynenko, D. et al. Magnetic skyrmion as a nonlinear resistive element: a potential building block for reservoir computing. *Phys. Rev. Appl.* **9**, 014034 (2018).
8. Song, K. M. et al. Skyrmion-based artificial synapses for neuromorphic computing. *Nat. Electron.* **3**, 148–155 (2020).
9. Yokouchi, T. et al. Pattern recognition with neuromorphic computing using magnetic field–induced dynamics of skyrmions. *Sci. Adv.* **8**, eabq5652 (2022).
10. Kang, W. et al. Magnetic skyrmions for future potential memory and logic applications: alternative information carriers. In *2018 Design, Automation & Test in Europe Conference & Exhibition (DATE)* 119–124 (2018). https://doi.org/10.23919/DATE.2018.8341990.
11. Luo, S. & You, L. Skyrmion devices for memory and logic applications. *APL Mater.* **9**, 050901 (2021).
12. Psaroudaki, C. & Panagopoulos, C. Skyrmion qubits: a new class of quantum logic elements based on nanoscale magnetization. *Phys. Rev. Lett.* **127**, 067201 (2021).
13. Bessarab, P. F. et al. Lifetime of racetrack skyrmions. *Sci. Rep.* **8**, 3433 (2018).
14. Wright, D. C. & Mermin, N. D. Crystalline liquids: the blue phases. *Rev. Mod. Phys.* **61**, 385–432 (1989).
15. Mühlbauer, S. et al. Skyrmion lattice in a chiral magnet. *Science* **323**, 915–919 (2009).
16. Yu, X. Z. et al. Real-space observation of a two-dimensional skyrmion crystal. *Nature* **465**, 901–904 (2010).
17. Heinze, S. et al. Spontaneous atomic-scale magnetic skyrmion lattice in two dimensions. *Nat. Phys.* **7**, 713–718 (2011).
18. Soumyanarayanan, A. et al. Tunable room-temperature magnetic skyrmions in Ir/Fe/Co/Pt multilayers. *Nat. Mater.* **16**, 898–904 (2017).
19. Boulle, O. et al. Room-temperature chiral magnetic skyrmions in ultrathin magnetic nanostructures. *Nat. Nanotechnol.* **11**, 449–454 (2016).
20. Hallal, A. et al. Rashba-type Dzyaloshinskii–Moriya interaction, perpendicular magnetic anisotropy, and skyrmion states at 2D materials/co interfaces. *Nano Lett.* **21**, 7138–7144 (2021).
21. Romming, N. et al. Writing and deleting single magnetic skyrmions. *Science* **341**, 636–639 (2013).
22. Rana, K. G. et al. Room-temperature skyrmions at zero field in exchange-biased ultrathin films. *Phys. Rev. Appl.* **13**, 044079 (2020).
23. Zhang, H. et al. Room-temperature skyrmion lattice in a layered magnet $(Fe_{0.5}Co_{0.5})_5GeTe_2$. *Sci. Adv.* **8**, eabm7103 (2022).
24. Gallagher, J. C. et al. Robust zero-field skyrmion formation in FeGe epitaxial thin films. *Phys. Rev. Lett.* **118**, 027201 (2017).
25. Huang, B. et al. Layer-dependent ferromagnetism in a van der Waals crystal down to the monolayer limit. *Nature* **546**, 270–273 (2017).
26. Gong, C. et al. Discovery of intrinsic ferromagnetism in two-dimensional van der Waals crystals. *Nature* **546**, 265 (2017).
27. Ahn, E. C. 2D materials for spintronic devices. *Npj 2D Mater. Appl.* **4**, 1–14 (2020).
28. Hu, G. & Xiang, B. Recent advances in two-dimensional spintronics. *Nanoscale Res. Lett.* **15**, 226 (2020).
29. Elahi, E. et al. A review on two-dimensional (2D) magnetic materials and their potential applications in spintronics and spin-caloritronic. *Comput. Mater. Sci.* **213**, 111670 (2022).
30. Moon, K.-W., Yoon, J., Kim, C. & Hwang, C. Existence of in-plane magnetic skyrmion and its motion under current flow. *Phys. Rev. Appl.* **12**, 064054 (2019).
31. Yuan, J. et al. Intrinsic skyrmions in monolayer Janus magnets. *Phys. Rev. B* **101**, 094420 (2020).
32. Liang, J. et al. Very large Dzyaloshinskii-Moriya interaction in two-dimensional Janus manganese dichalcogenides and its application to realize skyrmion states. *Phys. Rev. B* **101**, 184401 (2020).
33. Shen, Z., Xue, Y., Wu, Z. & Song, C. Enhanced Curie temperature and skyrmion stability by strain in room temperature ferromagnetic semiconductor CrISe monolayer. *Appl. Phys. Lett.* **121**, 202402 (2022).
34. Zhang, Y. et al. Generation of magnetic skyrmions in two-dimensional magnets via interfacial proximity. *Phys. Rev. B* **107**, 024402 (2023).
35. Naguib, M. et al. Two-dimensional nanocrystals produced by exfoliation of Ti_3AlC_2. *Adv. Mater.* **23**, 4248–4253 (2011).
36. Anasori, B. et al. Control of electronic properties of 2D carbides (MXenes) by manipulating their transition metal layers. *Nanoscale Horiz.* **1**, 227–234 (2016).
37. Chaney, G., Çakır, D., Peeters, F. M. & Ataca, C. Stability of adsorption of Mg and Na on sulfur-functionalized MXenes. *Phys. Chem. Chem. Phys.* **23**, 25424–25433 (2021).
38. Xie, Y. et al. Role of surface structure on Li-Ion energy storage capacity of two-dimensional transition-metal carbides. *J. Am. Chem. Soc.* **136**, 6385–6394 (2014).
39. Jiang, X. et al. Two-dimensional MXenes: from morphological to optical, electric, and magnetic properties and applications. *Phys. Rep.* **848**, 1–58 (2020).
40. Deysher, G. et al. Synthesis of Mo_4VAlC_4 MAX phase and two-dimensional Mo_4VC_4 MXene with five atomic layers of transition metals. *ACS Nano* **14**, 204–217 (2020).
41. Hong, W., Wyatt, B. C., Nemani, S. K. & Anasori, B. Double transition-metal MXenes: atomistic design of two-dimensional carbides and nitrides. *MRS Bull.* **45**, 850–861 (2020).
42. Ding, H. et al. Chemical scissor–mediated structural editing of layered transition metal carbides. *Science* **379**, 1130–1135 (2023).
43. Rajan, A. C. et al. Machine-learning-assisted accurate band gap predictions of functionalized MXene. *Chem. Mater.* **30**, 4031–4038 (2018).
44. Haastrup, S. et al. The computational 2D materials database: high-throughput modeling and discovery of atomically thin crystals. *2D Mater.* **5**, 42002 (2018).
45. Gjerding, M. N. et al. Recent Progress of the Computational 2D Materials Database (C2DB). *2D Mater.* **8**, 44002 (2021).
46. Tan, T. L., Jin, H. M., Sullivan, M. B., Anasori, B. & Gogotsi, Y. High-throughput survey of ordering configurations in MXene alloys across compositions and temperatures. *ACS Nano* **11**, 4407–4418 (2017).
47. Guha, S., Kabiraj, A. & Mahapatra, S. High-throughput design of functional-engineered MXene transistors with low-resistive contacts. *Npj Comput. Mater.* **8**, 202 (2022).
48. Zheng, J. et al. High-throughput screening of hydrogen evolution reaction catalysts in MXene materials. *J. Phys. Chem. C.* **124**, 13695–13705 (2020).
49. Xiao, Y. & Zhang, W. High throughput screening of M_3C_2 MXenes for efficient CO_2 reduction conversion into hydrocarbon fuels. *Nanoscale* **12**, 7660–7673 (2020).
50. Mermin, N. D. & Wagner, H. Absence of ferromagnetism or antiferromagnetism in one- or two-dimensional isotropic Heisenberg models. *Phys. Rev. Lett.* **17**, 1133–1136 (1966).
51. Jenkins, S. et al. Breaking through the Mermin-Wagner limit in 2D van der Waals magnets. *Nat. Commun.* **13**, 6917 (2022).
52. Azadmanjiri, J., Roy, P. K., Děkanovský, L. & Sofer, Z. Chalcogen (S, Se, and Te) decorated few-layered Ti_3C_2Tx MXene hybrids: modulation of properties through covalent bonding. *Nanoscale* **15**, 4033–4044 (2023).
53. Gong, S. et al. Iodine-functionalized titanium carbide MXene with ultra-stable pseudocapacitor performance. *J. Colloid Interface Sci.* **615**, 643–649 (2022).
54. Kabiraj, A., Kumar, M. & Mahapatra, S. High-throughput discovery of high Curie point two-dimensional ferromagnetic materials. *Npj Comput. Mater.* **6**, 35 (2020).
55. Kabiraj, A., Jain, T. & Mahapatra, S. Massive Monte Carlo simulations-guided interpretable learning of two-dimensional Curie temperature. *Patterns* **3**, 100625 (2022).
56. Tsuneda, T. & Hirao, K. Self-interaction corrections in density functional theory. *J. Chem. Phys.* **140**, 18A513 (2014).
57. Moore, G. C., Horton, M. K., Ganose, A. M., Siron, M. & Persson, K. A. High-throughput determination of Hubbard U and Hund J values for transition metal oxides via linear response formalism. Preprint at https://arxiv.org/abs/2201.04213 (2022).
58. Sun, J., Ruzsinszky, A. & Perdew, J. P. Strongly constrained and appropriately normed semilocal density functional. *Phys. Rev. Lett.* **115**, 36402 (2015).
59. Sun, J. et al. Accurate first-principles structures and energies of diversely bonded systems from an efficient density functional. *Nat. Chem.* **8**, 831–836 (2016).
60. Chakraborty, A., Dixit, M., Aurbach, D. & Major, D. T. Predicting accurate cathode properties of layered oxide materials using the SCAN meta-GGA density functional. *Npj Comput. Mater.* **4**, 60 (2018).
61. Devi, R., Singh, B., Canepa, P. & Sai Gautam, G. Effect of exchange-correlation functionals on the estimation of migration barriers in battery materials. *Npj Comput. Mater.* **8**, 160 (2022).
62. Furness, J. W., Kaplan, A. D., Ning, J., Perdew, J. P. & Sun, J. Accurate and numerically efficient r^2SCAN meta-generalized gradient approximation. *J. Phys. Chem. Lett.* **11**, 8208–8215 (2020).
63. Kingsbury, R. et al. Performance comparison of r^2SCAN and SCAN metaGGA density functionals for solid materials via an automated, high-throughput computational workflow. *Phys. Rev. Mater.* **6**, 013801 (2022).
64. Zhang, X., Zhou, Y. & Ezawa, M. Antiferromagnetic skyrmion: stability, creation and manipulation. *Sci. Rep.* **6**, 1–8 (2016).
65. Kim, S. K., Lee, K.-J. & Tserkovnyak, Y. Self-focusing skyrmion racetracks in ferrimagnets. *Phys. Rev. B* **95**, 140404 (2017).
66. Yang, H., Thiaville, A., Rohart, S., Fert, A. & Chshiev, M. Anatomy of Dzyaloshinskii-Moriya Interaction at Co/Pt Interfaces. *Phys. Rev. Lett.* **115**, 267210 (2015).
67. Müller, G. P. et al. Spirit: multifunctional framework for atomistic spin simulations. *Phys. Rev. B* **99**, 1–16 (2019).
68. Fert, A., Cros, V. & Sampaio, J. Skyrmions on the track. *Nat. Nanotechnol.* **8**, 152–156 (2013).
69. Torelli, D. & Olsen, T. Calculating critical temperatures for ferromagnetic order in two-dimensional materials. *2D Mater.* **6**, 15028 (2018).
70. Lu, X., Fei, R. & Yang, L. Curie temperature of emerging two-dimensional magnetic structures. *Phys. Rev. B* **100**, 205409 (2019).
71. Torelli, D., Thygesen, K. S. & Olsen, T. High throughput computational screening for 2D ferromagnetic materials: the critical role of anisotropy and local correlations. *2D Mater.* **6**, 045018 (2019).

72. Xiang, H. J., Kan, E. J., Wei, S.-H., Whangbo, M.-H. & Gong, X. G. Predicting the spin-lattice order of frustrated systems from first principles. *Phys. Rev. B* **84**, 224429 (2011).
73. Arpaci, S. et al. Observation of current-induced switching in non-collinear antiferromagnetic $IrMn_3$ by differential voltage measurements. *Nat. Commun.* **12**, 3828 (2021).
74. Deng, Y. et al. Gate-tunable room-temperature ferromagnetism in two-dimensional Fe_3GeTe_2. *Nature* **563**, 94–99 (2018).
75. Tiwari, S., Vanherck, J., Van de Put, M. L., Vandenberghe, W. G. & Sorée, B. Computing Curie temperature of two-dimensional ferromagnets in the presence of exchange anisotropy. *Phys. Rev. Res.* **3**, 1–10 (2021).
76. Vansteenkiste, A. et al. The design and verification of MuMax3. *AIP Adv.* **4**, 107133 (2014).
77. Alameda, L. T., Moradifar, P., Metzger, Z. P., Alem, N. & Schaak, R. E. Topochemical deintercalation of Al from MoAlB: stepwise etching pathway, layered intergrowth structures, and two-dimensional MBene. *J. Am. Chem. Soc.* **140**, 8833–8840 (2018).
78. Zhang, H., Xiang, H., Dai, F., Zhang, Z. & Zhou, Y. First demonstration of possible two-dimensional MBene CrB derived from MAB phase Cr_2AlB_2. *J. Mater. Sci. Technol.* **34**, 2022–2026 (2018).
79. Zhang, B., Zhou, J. & Sun, Z. MBenes: progress, challenges and future. *J. Mater. Chem. A* **10**, 15865–15880 (2022).
80. Osanloo, M. R., Van de Put, M. L., Saadat, A. & Vandenberghe, W. G. Identification of two-dimensional layered dielectrics from first principles. *Nat. Commun.* **12**, 5051 (2021).
81. Zimmermann, B. et al. Comparison of first-principles methods to extract magnetic parameters in ultrathin films: Co/Pt(111). *Phys. Rev. B* **99**, 214426 (2019).
82. Kresse, G. & Hafner, J. Ab initio molecular dynamics for liquid metals. *Phys. Rev. B* **47**, 558–561 (1993).
83. Kresse, G. & Hafner, J. Ab initio molecular-dynamics simulation of the liquid-metal–amorphous-semiconductor transition in germanium. *Phys. Rev. B* **49**, 14251–14269 (1994).
84. Kresse, G. & Furthmüller, J. Efficient iterative schemes for ab initio total-energy calculations using a plane-wave basis set. *Phys. Rev. B* **54**, 11169–11186 (1996).
85. Kresse, G. & Furthmüller, J. Efficiency of ab-initio total energy calculations for metals and semiconductors using a plane-wave basis set. *Comput. Mater. Sci.* **6**, 15–50 (1996).
86. Kresse, G. & Joubert, D. From ultrasoft pseudopotentials to the projector augmented-wave method. *Phys. Rev. B* **59**, 1758–1775 (1999).
87. Jain, A. et al. Commentary: the materials project: a materials genome approach to accelerating materials innovation. *APL Mater.* **1**, 11002 (2013).
88. Momma, K. & Izumi, F. VESTA 3 for three-dimensional visualization of crystal, volumetric and morphology data. *J. Appl. Crystallogr.* **44**, 1272–1276 (2011).
89. Ning, J. et al. Workhorse minimally empirical dispersion-corrected density functional with tests for weakly bound systems: r^2SCAN+rVV10. *Phys. Rev. B* **106**, 075422 (2022).
90. Ong, S. P. et al. Python materials genomics (pymatgen): a robust, open-source python library for materials analysis. *Comput. Mater. Sci.* **68**, 314–319 (2013).
91. Hjorth Larsen, A. et al. The atomic simulation environment—a Python library for working with atoms. *J. Phys. Condens. Matter* **29**, 273002 (2017).
92. Liu, J., Shi, M., Lu, J. & Anantram, M. P. Analysis of electrical-field-dependent Dzyaloshinskii-Moriya interaction and magnetocrystalline anisotropy in a two-dimensional ferromagnetic monolayer. *Phys. Rev. B* **97**, 054416 (2018).
93. Tang, W., Sanville, E. & Henkelman, G. A grid-based Bader analysis algorithm without lattice bias. *J. Phys. Condens. Matter* **21**, 84204 (2009).
94. Sanville, E., Kenny, S. D., Smith, R. & Henkelman, G. Improved grid-based algorithm for Bader charge allocation. *J. Comput. Chem.* **28**, 899–908 (2007).
95. Henkelman, G., Arnaldsson, A. & Jónsson, H. A fast and robust algorithm for Bader decomposition of charge density. *Comput. Mater. Sci.* **36**, 354–360 (2006).

ACKNOWLEDGEMENTS

The authors would like to express their heartfelt gratitude to the Centre for Development of Advanced Computing (C-DAC) in India for providing access to the cutting-edge PARAM Siddhi-AI supercomputer and extending a full waiver of the huge computational charges incurred in this work. Fellowship of AK was supported by the Core Research Grant (CRG) scheme of the Science and Engineering Research Board (SERB), Government of India, under Grant No. CRG/2020/000758. Authors strongly believe that such curiosity driven research can only foster in subsidized academic system.

AUTHOR CONTRIBUTIONS

A.K. conceived the problem statement, developed the high-throughput methodology and the codes, performed the calculations, analyzed the results, and wrote the first draft. S.M. acquired the fundings, finalized the manuscript, and overall supervised the work. Both authors designed the graphics.

COMPETING INTERESTS

The authors declare no competing interests.

ADDITIONAL INFORMATION

Supplementary information The online version contains supplementary material available at https://doi.org/10.1038/s41524-023-01129-x.

Correspondence and requests for materials should be addressed to Santanu Mahapatra.

Reprints and permission information is available at http://www.nature.com/reprints

Publisher's note Springer Nature remains neutral with regard to jurisdictional claims in published maps and institutional affiliations.

Open Access This article is licensed under a Creative Commons Attribution 4.0 International License, which permits use, sharing, adaptation, distribution and reproduction in any medium or format, as long as you give appropriate credit to the original author(s) and the source, provide a link to the Creative Commons license, and indicate if changes were made. The images or other third party material in this article are included in the article's Creative Commons license, unless indicated otherwise in a credit line to the material. If material is not included in the article's Creative Commons license and your intended use is not permitted by statutory regulation or exceeds the permitted use, you will need to obtain permission directly from the copyright holder. To view a copy of this license, visit http://creativecommons.org/licenses/by/4.0/.

© The Author(s) 2023